



## Highly efficient and stable Ru/K-OMS-2 catalyst for NO oxidation



S. Adjimi<sup>a,b</sup>, J.M. García-Vargas<sup>a</sup>, J.A. Díaz<sup>a</sup>, L. Retailleau<sup>a</sup>, S. Gil<sup>a</sup>, M. Pera-Titus<sup>c</sup>, Y. Guo<sup>b</sup>, A. Giroir-Fendler<sup>a,\*</sup>

<sup>a</sup> Univ Lyon, Université Claude Bernard Lyon 1, CNRS, IRCELYON, 2 Avenue Albert Einstein, Villeurbanne, F-69622, France

<sup>b</sup> Key Laboratory for Advanced Materials, Research Institute of Industrial Catalysis, School of Chemistry and Molecular Engineering, East China University of Science and Technology, Shanghai 200237, China

<sup>c</sup> Eco-Efficient Products and Processes Laboratory (E2P2L), UMI 3464 CNRS—Solvay, 3066 Jin Du Road, Xin Zhuang Ind. Zone, 201108 Shanghai, China

### ARTICLE INFO

#### Article history:

Received 10 May 2017

Received in revised form 11 July 2017

Accepted 15 July 2017

Available online 18 July 2017

#### Keywords:

OMS-2

Ruthenium

NO oxidation

Fast SCR

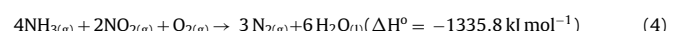
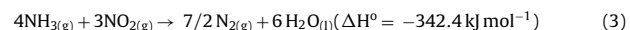
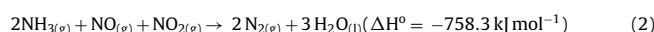
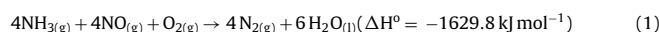
### ABSTRACT

The influence of addition of a series of non noble and noble metals to a manganese oxide octahedral molecular sieve (OMS) with a cryptomelane structure (K-OMS-2) has been studied for NO oxidation in view of fast selective catalytic reduction applications. Fe, Cu, Zn, Pt, Pd, Ru and Ag were selected as dopant metals with a metal loading around 2 wt.%. The catalysts were characterized in detail by ICP-OES, N<sub>2</sub> adsorption/desorption at 77 K, XRD, H<sub>2</sub>-TPR and HR-TEM. The highest NO conversion was obtained for a K-OMS-2 catalyst modified with ruthenium, showing a reaction rate up to 5.3 μmol g<sup>-1</sup> s<sup>-1</sup> at 584 K. A markedly higher catalyst reducibility upon incorporation of ruthenium can be proposed as an underlying reason for the enhanced catalytic performance.

© 2017 Elsevier B.V. All rights reserved.

## 1. Introduction

The combustion of fossil fuels is one of the main emission sources of atmospheric pollutants. These pollutants include not only CO<sub>2</sub> and CH<sub>4</sub>, but also a panel of nitrogen oxides (e.g., N<sub>2</sub>O, NO, NO<sub>2</sub>) that contribute to the greenhouse effect and take part in photochemical reactions leading to tropospheric ozone and acid rain formation [1,2]. The abatement of nitrogen oxides (NO<sub>x</sub>) has been achieved in gasoline cars using the so-called “Three Way Catalysts” (TWC), but this technology can be hardly employed for Diesel engines due to the high oxygen concentration in the exhaust gases. To overcome this shortcoming, specific aftertreatment processes have been developed, such as the Selective Catalytic Reduction (SCR). In this technology, the addition of a reducing agent (most often NH<sub>3</sub>) combined with a proper catalyst can mitigate NO<sub>x</sub> emissions down to the legal limits in the presence of O<sub>2</sub>. The main reactions involved in the NH<sub>3</sub>-SCR process are listed below (Eqs. (1)–(4)) [3]:



Noteworthy, NO<sub>2</sub> is required in most of these reactions (Eqs. (2)–(4)). It is especially important the contribution of Eq. (2), also known as Fast SCR, showing a reaction rate about 10 times faster than Eq. (2) in the presence of equimolar amounts of NO and NO<sub>2</sub>. However, since NO<sub>x</sub> typically consists of >90% NO under standard combustion conditions [4,5], reaction (1) dominates. As an attempt to make NH<sub>3</sub>-SCR in Diesel engine aftertreatment processes more efficient, one could think about the combination of a first catalytic step boosting the partial oxidation of NO to reach a NO/NO<sub>2</sub> ratio close to 1 followed by a fast SCR unit favoring reaction (2).

OMS-2 materials (also termed cryptomelanes or hollandites) are based on edge-shared MnO<sub>6</sub> octahedra hosting both Mn(III) and Mn(IV) and 2 × 2 1D microtunnels with 4.6 × 4.6 Å dimensions, an average oxidation state of Mn about 3.8 and incorporating ex-framework compensation cations (usually K<sup>+</sup>) [6–8]. Cryptomelanes have been widely explored as catalysts due to their unique porous structure, mild surface acid-base properties and ion-exchange capacity [9–11]. In particular, cryptomelanes have shown high activity and stability in the total oxidation of CO [12–14] and VOCs [15–19], as well as in partial oxidation [20–26], epoxidation [27–30] and selective hydrogenation reactions [31,32]. The high activity observed in oxidative/reductive reactions is usually attributed to the presence of Mn in different oxidation

\* Corresponding author.

E-mail address: [anne.giroir-fendler@ircelyon.univ-lyon1.fr](mailto:anne.giroir-fendler@ircelyon.univ-lyon1.fr) (A. Giroir-Fendler).

**Table 1**

Physicochemical properties of the metal-loaded K-OMS-2 catalysts.

Sample	M/K-OMS-2							
	Parent	M = Fe	M = Cu	M = Zn	M = Pt	M = Pd	M = Ru	M = Ag
Mn loading (wt.%)	55.93	—	—	—	—	—	—	—
Metal loading (wt.%)	—	2.68	1.42	1.30	1.73	2.31	1.67	2.54
Surface area ( $\text{m}^2 \text{ g}^{-1}$ )	85	80	84	83	91	83	82	81
Pore volume ( $\text{cm}^3 \text{ g}^{-1}$ )	0.393	0.381	0.388	0.391	0.394	0.375	0.412	0.388
$\text{H}_2$ uptake ( $\text{mmol g}^{-1}$ )	9.44	—	—	—	9.90	—	10.19	9.04
Mean particle size OMS (XRD, nm)	11.7	16.5	12.9	15.0	12.4	14.9	12.1	14.0
Mean particle size metal (HR-TEM, nm)	—	—	—	—	3.9	4.9	2.1	13.3

states, forming different redox couples ( $\text{Mn}^{4+}/\text{Mn}^{3+}$ ;  $\text{Mn}^{4+}/\text{Mn}^{2+}$ ), and to the presence of lattice oxygen with high mobility and reactivity [21,33], favoring Mars van Krevelen mechanisms [21]. These materials have also been explored as catalytic supports, showing a tunable morphology and performance upon addition of noble [12,13,18,26,31,32,34–36] and non noble metals [14,19,24,30,37–39] either as cations hosted in the tunnels or partially exchanged into the framework, or in the form of supported nanoparticles. The presence of metals in the cryptomelane framework can alter the average oxidation state of Mn and the mobility of the lattice oxygen, modifying the catalytic performance of this material not only because of the contribution of the metal particles but also because of the different chemical and physical properties of the modified cryptomelane [40].

The studies focusing on the adsorption and catalytic properties of cryptomelanes with  $\text{NO}_x$  are scarce. It is known that NO can adsorb in the cryptomelane framework, but only at the external surface and as a function of the cation loading and water loading [41,42]. The adsorption uptake can be promoted by the simultaneous oxidation with lattice oxygen, encompassing the partial reduction of the cryptomelane framework. This adsorption pattern opposes to that of  $\text{NH}_3$ , which can adsorb in the cryptomelane channels in strong synergy with cations (preferentially  $\text{H}^+$ ) and bounded water [43]. The oxidation of  $\text{NH}_3$  with NO at low temperature (473 K) was reported to proceed over H-OMS-2, but with low selectivity to  $\text{N}_2$  [44]. The selective  $\text{NH}_3$  oxidation into  $\text{N}_2$  under  $\text{O}_2$  also proceeded over V-substituted K-OMS-2 at 423 K, but only at very high V loading (V/Mn = 10%) [45]. Finally, CuO/OMS-2 afforded the almost complete reduction of NO into  $\text{N}_2$  using CO as reducing agent at a temperature higher than 500 K [46].

On the guidance of these earlier studies, herein we report the catalytic performance of a series of metal-functionalized manganese octahedral molecular sieves with cryptomelane framework (i.e. K-OMS-2) for NO oxidation at exhaust gas conditions in view of fast  $\text{NH}_3$ -SCR applications.

## 2. Experimental

### 2.1. Materials

Manganese sulfate hydrate ( $\text{MnSO}_4 \cdot \text{H}_2\text{O}$ , 99.5%) and potassium permanganate ( $\text{KMnO}_4$ , 99.5%), both supplied by Sigma-Aldrich, were used as reactants for the synthesis of K-OMS-2. Manganese oxide ( $\text{MnO}_2$ , 99%) used as catalyst was supplied by Sigma-Aldrich.  $\text{La}(\text{NO}_3)_3 \cdot 6\text{H}_2\text{O}$  (Sigma Aldrich, >99.0%),  $\text{Mn}(\text{NO}_3)_2 \cdot 4\text{H}_2\text{O}$  (Alfa Aesar, 98%) and citric acid (CA) (Alfa Aesar, >99.5%) of analytical grade were used as precursors for the synthesis of  $\text{LaMnO}_3$  perovskite-type oxides.

### 2.2. Catalyst synthesis

K-OMS-2 manganese octahedral molecular sieve was prepared by the reflux method [47]. Briefly, an aqueous solution of  $\text{KMnO}_4$

(5.8 g in 100 mL deionized water) was added to a solution of  $\text{MnSO}_4 \cdot \text{H}_2\text{O}$  (8.8 g in 30 mL deionized water) and concentrated nitric acid (3 mL). The mixture was refluxed at 100 °C for 24 h. After the synthesis, the dark brown solid was filtered, washed with deionized water until neutral pH, and dried overnight at 120 °C before use.

The parent K-OMS-2 support was subsequently doped with different metals (nominal loading = 2 wt.%) using the ion exchange procedure (Table 1). A diluted aqueous solution ( $10^{-4}$  M) of the corresponding metal precursor,  $\text{M}(\text{NH}_3)_4(\text{NO}_3)_x$  was mixed with the as-prepared K-OMS-2 at 80 °C for 2 h under  $\text{N}_2$  atmosphere. Using this method, a series of catalysts containing Pt, Pd, Ru, Ag, Fe, Cu and Zn were prepared. After the synthesis, the samples were submitted to vacuum evaporation (150 mbar) at 70 °C followed by drying overnight at 100 °C and calcination at 300 °C for 2 h under air. The different catalysts were labeled as X/K-OMS-2, where X stands for the metal dopant.

The  $\text{LaMnO}_3$  perovskite was prepared by the citrate sol-gel method. First, an aqueous solution based on equimolar amounts of the nitrate precursors was prepared. Then, citric acid (CA) was added at room temperature and the molar ratio of CA to total metallic ions (sum of  $\text{La}^{3+}$  and  $\text{Mn}^{2+}$ ) set at 1.2 (pH = 1). The final solution was heated to 80 °C for 2 h using magnetic stirring, then the solid was recovered and dried at 120 °C overnight. The resulting solid was then subjected to thermal treatment in a muffle furnace at 200 °C for 1 h (heating rate of  $2^\circ\text{C min}^{-1}$ ) and was finally *in situ* calcined at 750 °C for 2 h (heating rate of  $5^\circ\text{C min}^{-1}$ ) in the quartz tubular reactor under air atmosphere.

### 2.3. Catalyst characterization

The bulk metal composition of the different samples was quantified by inductively coupled plasma analysis (ICP) using an Activa (Horiba Jobin-Yvon) Optical Emission Spectrometer. Before the measurements, the samples were dissolved using a mixture of inorganic acids ( $\text{H}_2\text{SO}_4$ ,  $\text{HNO}_3$  and HF).

The specific surface area and pore volume of the different catalysts was measured from  $\text{N}_2$  adsorption/desorption isotherms at 77.4 K using a Micromeritics ASAP 2010 Surface Area Analyzer. The surface areas were calculated by the Brunauer-Emmett-Teller (BET) method in the relative pressure range  $0.05 < \text{P}/\text{P}_0 < 0.25$ , while the pore volumes were measured at  $\text{P}/\text{P}_0 = 0.99$ . The Barrer-Joyner-Halenda (BJH) method was used for measuring intercrystalline mean pore sizes. Prior to the measurements, the catalysts were degassed at 473 K under vacuum during 15 h.

The phases present in the different catalysts were analyzed by powder X-ray diffraction (PXRD). The PXRD patterns were recorded on a Bruker D5005 diffractometer provided with  $\text{Cu-K}\alpha$  radiation ( $\lambda = 1.5418 \text{ \AA}$ ) in the  $2\theta$  range of  $8$ – $80^\circ$  with a step size of  $0.05^\circ$ . The patterns were indexed using the Joint Committee on Powder Diffraction (JCPDS) database.

The morphology and structure of the catalysts was inspected by Transmission Electron Microscopy (HR-TEM) on a JEOL 2010

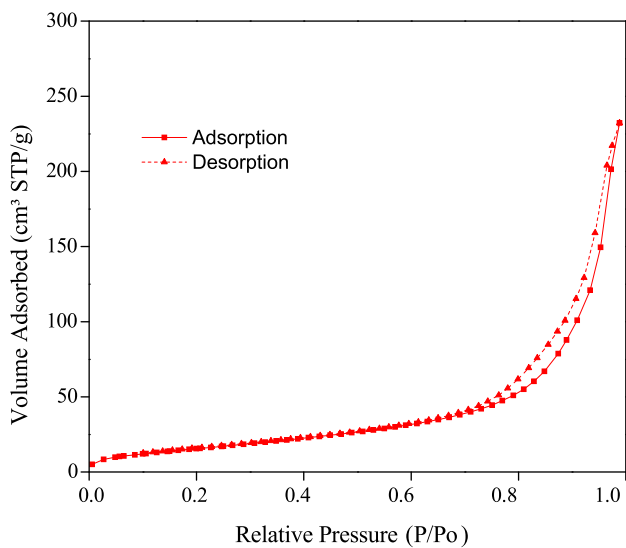


**Fig. 1.**  $\text{N}_2$  Adsorption-desorption isotherm at 77 K for K-OMS-2.

LaB6 microscope using an acceleration voltage of 200 kV with LaB6 emission and a point resolution of 0.19 nm. Standard holey carbon-covered copper TEM grids were used for supporting the catalyst samples previously crushed in ethanol. The mean metal particle size for the K-OMS-2 support and metal nanoparticles was measured for the different catalysts as a surface-area weighted diameter ( $\bar{d}_s$ ) as follows

$$\bar{d}_s = \frac{\sum n_i d_i^3}{\frac{i}{n_i d_i^2}} \quad (5)$$

where  $n_i$  represents the number of particles with diameter  $d_i$  ( $\sum n_i \geq 200$ ).

Temperature-programmed reduction (TPR) experiments were conducted on a homemade setup equipped with a VG Gaslab 300 quadrupole mass spectrometer. The signal at  $m/e = 2$ , corresponding to  $\text{H}_2^+$  ion was recorded during the heating ramp. The samples (ca. 20 mg) were loaded into a U-shaped quartz tube and pre-treated under He atmosphere at 523 K for 1 h. After cooling down to room temperature, the samples were ramped from room temperature to 973 K ( $10 \text{ K min}^{-1}$ ), using a reducing gas mixture of 1% v/v  $\text{H}_2/\text{He}$  ( $45 \text{ cm}^3 (\text{STP}) \cdot \text{min}^{-1}$ ).

#### 2.4. Catalytic activity measurements

The catalytic tests for NO oxidation over the parent and metal-doped K-OMS-2 catalysts were carried out in a fixed-bed quartz reactor ( $\phi = 6 \text{ mm}$ , length = 1 cm) at atmospheric pressure using silicon carbide (SiC) as diluent and a catalyst weight ensuring 0.174 mmol Mn (16 mg of catalyst unless otherwise stated). The inlet gas was composed of 1000 ppm NO, 8% O<sub>2</sub> and balance Ar. The gas hourly space velocity (GHSV) was set at 35,000 h<sup>-1</sup> for all experiments. The NO and NO<sub>2</sub> concentration at the outlet of the reactor was analyzed using a ThermoFisher NO/NO<sub>x</sub> chemiluminescence system equipped with a trap before the detector. Comprehensive reproducibility tests were performed for all samples, whereas the stability was surveyed in detail for the most performing catalysts. The catalytic activity was evaluated on the basis of light off experiments at atmospheric pressure from room temperature to 800 K using a heating ramp of 2 K min<sup>-1</sup>. The NO conversion and the reac-

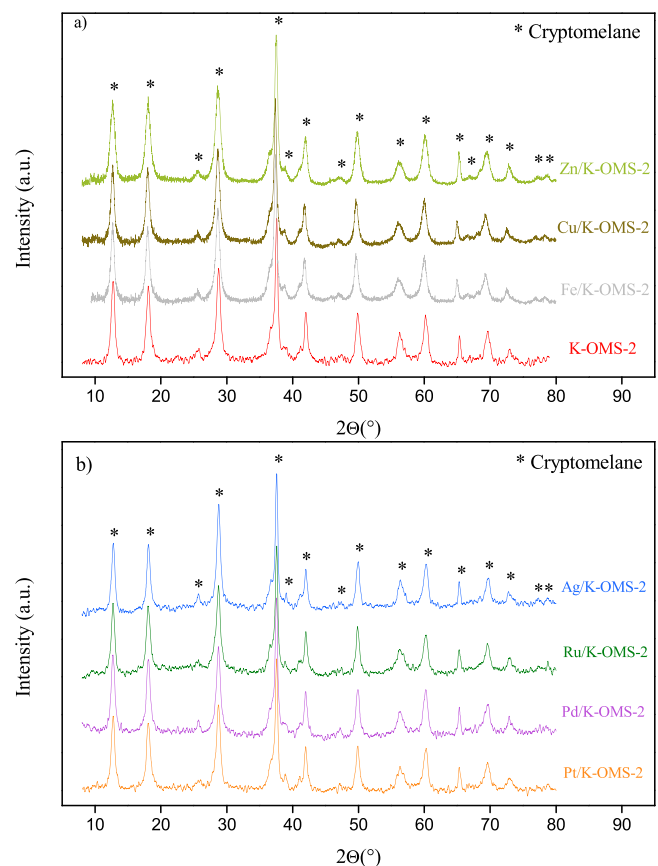


**Fig. 2.** XRD patterns of a) parent K-OMS-2 and K-OMS-2 loaded with non-noble metals, and b) K-OMS-2 loaded with noble metals.

tion rate for NO oxidation as a function of temperature [ $r_{\text{NO}}(T)$ ] were calculated as follows:

$$\text{NO conversion} = 1 - \frac{\text{outlet molar NO flow}}{\text{inlet molar NO flow}} \quad (6)$$

$$r_{\text{NO}}(T) = \frac{V_{\text{cat}} \text{ GHSV}}{24.4 m_{\text{cat}}} C_{\text{NO}}^0 X_{\text{NO}}(T) \quad (7)$$

where  $V_{\text{cat}}$  is the bulk volume of catalyst (L) in each experiment,  $C_{\text{NO}}^0$  is the NO concentration at the reactor inlet (ppm · 10<sup>-6</sup>),  $m_{\text{cat}}$  is the catalyst weight (0.016 g unless otherwise specified) and  $X_{\text{NO}}$  is the NO conversion. A blank experiment carried out with pure SiC showed no NO conversion under the experimental conditions here considered.

## 3. Results and discussion

### 3.1. Catalyst characterization

#### 3.1.1. Surface area and porosity

**Fig. 1** plots the  $\text{N}_2$  adsorption/desorption isotherms at 77 K for the fresh K-OMS-2 catalyst. A Type II–IV sorption pattern can be observed which can be attributed to  $\text{N}_2$  adsorption at the external surface of the particles, but with negligible adsorption in the microporous channels due to hindered  $\text{N}_2$  diffusion [10]. A H3-type hysteresis loop is also visible between the adsorption and desorption branches for  $P/P_0 > 0.6$  which can be associated to mesopores between nearby particles with non uniform size or shapes. The parent K-OMS-2 shows a BET specific surface area of  $85 \text{ m}^2 \text{ g}^{-1}$ , a total pore volume of  $0.393 \text{ cm}^3 \text{ g}^{-1}$  and a BJH pore size estimated from the adsorption curve about 16 nm. The measured BET surface areas are in good agreement with the theoretical values which

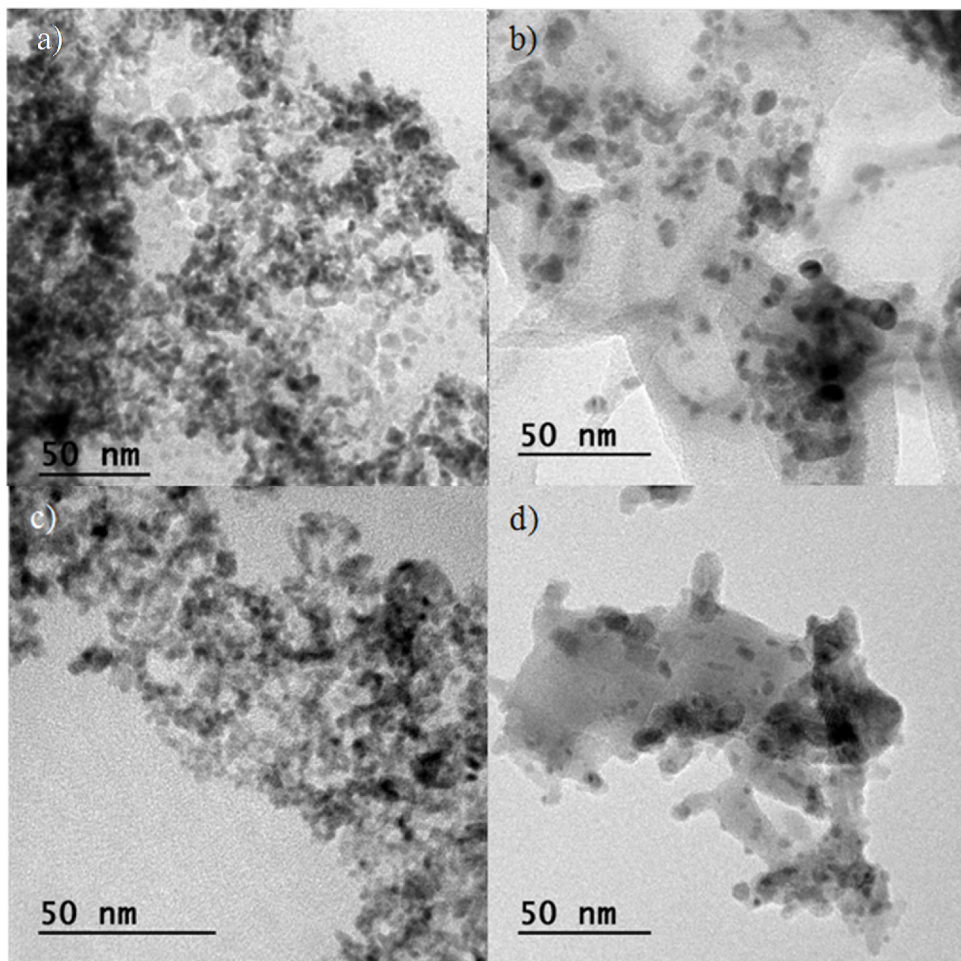


**Fig. 3.** TEM micrographs for: a) Pt/K-OMS-2, b) Pd/K-OMS-2, c) Ru/K-OMS-2 and d) Ag/K-OMS-2.

can be deduced from the crystallite size, about  $60\text{ m}^2\text{ g}^{-1}$  assuming a spherical shape and taking a density of  $4.3\text{ g cm}^{-3}$  for all samples [48]. No clear differences are observed in the textural properties between the metal-loaded catalysts and the parent K-OMS-2 (Table 1).

### 3.1.2. XRD patterns

Fig. 2 plots the XRD patterns of the different catalysts prepared in this study. In all cases, the XRD patterns exhibit characteristic (110), (200), (220), (310), (211), (301), (411), (600), (521), (002), (541), (312), (402) and (332) reflections belonging, respectively, to 2-theta angles 12.7, 18.0, 22.0, 28.7, 37.4, 42.0, 49.8, 56.1, 60, 65.3, 69.3, 73.1, 77.5, 78.7° which can be attributed to cryptomelane ( $\text{KMn}_8\text{O}_{16}$ , JCPDS No: 42-1348, I4/m tetragonal unit cell) with no indication of other phase impurities attributed to manganese oxides. No characteristic reflections can be observed for the metal phases, suggesting a good dispersion either as small metal nanoparticles or as cations integrated into the manganese framework. The mean crystallite size computed using the Debye-Scherrer equation for the strongest reflection (211) (2-theta = 37.4°) is 11.7 nm (Table 1). The mean size of the OMS particles increases after the metal addition, especially in the case of Fe, Zn and Pd, whereas the OMS particle size for Ru keeps almost unchanged.

### 3.1.3. HR-TEM images

The morphology of the metal-loaded K-OMS-2 catalysts was inspected by HR-TEM (Fig. 3). In all cases, a good dispersion of the metal phase can be observed. The mean particle size for the metal

nanoparticles measured after a statistical analysis of a representative number of micrographs for the different samples reveals a mean particle size of 3.9 nm, 4.9 nm, 2.1 nm and 13.3 nm for Pt/K-OMS-2, Pd/K-OMS-2, Ru/K-OMS-2 and Ag/K-OMS-2 (Table 1). In any case, no large metal agglomerates are observed.

### 3.1.4. $\text{H}_2$ -TPR profiles

The  $\text{H}_2$ -TPR profiles of the parent K-OMS-2 and Pt, Ru and Ag-loaded K-OMS-2 samples are plotted in Fig. 4, while the corresponding  $\text{H}_2$  consumption are listed in Table 1. The parent K-OMS-2 displays a broad peak in the temperature range 500–700 K which is composed of two overlapping peaks. These peaks can be attributed to the two-step reduction of K-OMS-2 to  $\text{Mn}_3\text{O}_4$  and further  $\text{Mn}_3\text{O}_4$  to  $\text{MnO}$  at higher temperature [49,50]. The maximum rate of reduction is observed in the temperature range 620–680 K. Although no information regarding the oxidation state of Mn can be unambiguously inferred from the  $\text{H}_2$  consumption, the measured value ( $9.44\text{ mmol g}^{-1}$ ) is near yet 18% lower than the expected value for complete reduction of  $\text{MnO}_2$  to  $\text{MnO}$  ( $11.5\text{ mmol g}^{-1}$ ).

The reduction behavior of K-OMS-2 shows a shift towards lower temperatures after metal doping. This shift becomes more pronounced for Pt/K-OMS-2, showing a maximum rate of reduction in the range 390–470 K, but with a comparable  $\text{H}_2$  consumption as for the parent K-OMS-2 (Table 1). This observation is classically attributed to the formation of hydrides over noble metal islands (in this case Pt), transferring fast to the  $\text{MnO}_x$  phase by spillover and favoring accordingly its reduction [51]. The reduction profile of this catalyst shows more clearly the two overlapped peaks

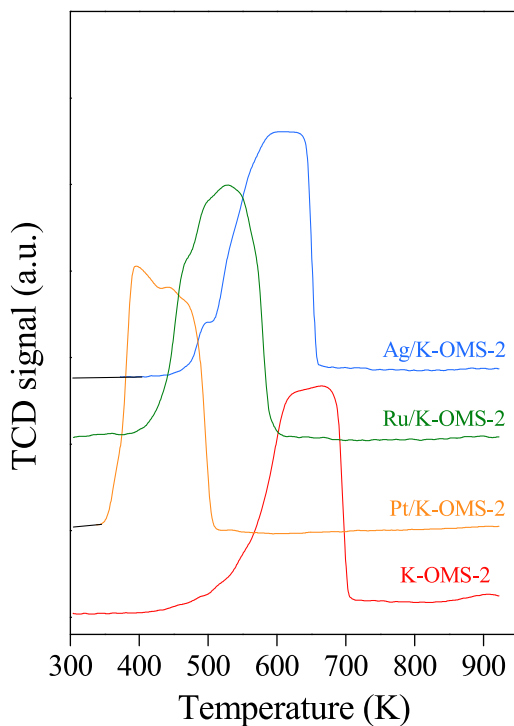


**Fig. 4.** H<sub>2</sub>-TPR profiles for: K-OMS-2, Pt/K-OMS-2, Ru/K-OMS-2 and Ag/K-OMS-2.

with peak maxima located at 400 K and 450 K, respectively. The incorporation of Ru also enhances the K-OMS-2 reducibility with a maximum reduction rate appearing in the temperature range 490–560 K and a H<sub>2</sub> consumption of 10.2 mmol g<sup>-1</sup>. Finally, Ag/K-OMS-2 displays the largest temperature range for the maximum rate of reduction (580–645 K) and a slight decline in the H<sub>2</sub> consumption (9.04 mmol g<sup>-1</sup>) compared to the value measured on K-OMS-2. In all cases, no reduction peak ascribed only to the metal phase can be visualized.

### 3.2. Catalytic activity for NO oxidation

#### 3.2.1. Catalytic activity of K-OMS-2 vs. LaMnO<sub>3</sub> and MnO<sub>2</sub>

The catalytic activity of the parent K-OMS-2 was first tested and compared to that of LaMnO<sub>3</sub> and commercial MnO<sub>2</sub>, used here as benchmarks, for NO oxidation into NO<sub>2</sub> from room temperature to 800 K. Fig. 5 plots the evolution of the NO conversion as a function of temperature. To our surprise, MnO<sub>2</sub> exhibits an almost negligible activity. In contrast, for K-OMS-2 and LaMnO<sub>3</sub>, the NO conversion increases first with the temperature until a maximum at about 641 K followed by a fast decline upon reaching the thermodynamic equilibrium (Fig. 5a). Despite this similar behavior, K-OMS-2 shows enhanced reaction rates in the whole temperature range with a rate up to 4.1 μmol g<sup>-1</sup> s<sup>-1</sup>, whereas the rate for LaMnO<sub>3</sub> is 1.6 μmol g<sup>-1</sup> s<sup>-1</sup>. Further analysis of the Arrhenius plots representing the evolution of the reaction rate with the inverse of temperature reveals a very similar activation energy for both catalysts (49 kJ mol<sup>-1</sup> for K-OMS-2 vs. 42 kJ mol<sup>-1</sup> for LaMnO<sub>3</sub>) (Fig. 5b). The activation energy measured for LaMnO<sub>3</sub> agrees well with the value reported by Chen et al. [52] at similar reaction conditions.

#### 3.2.2. Effect of non-noble metals on the catalytic activity of K-OMS-2

Given the prominent activity obtained for K-OMS-2 for NO oxidation, we assessed the influence of non-noble metal dopants on the catalytic properties. Fig. 6 plots the evolution of the NO conversion as a function of temperature. In line with the activity pattern

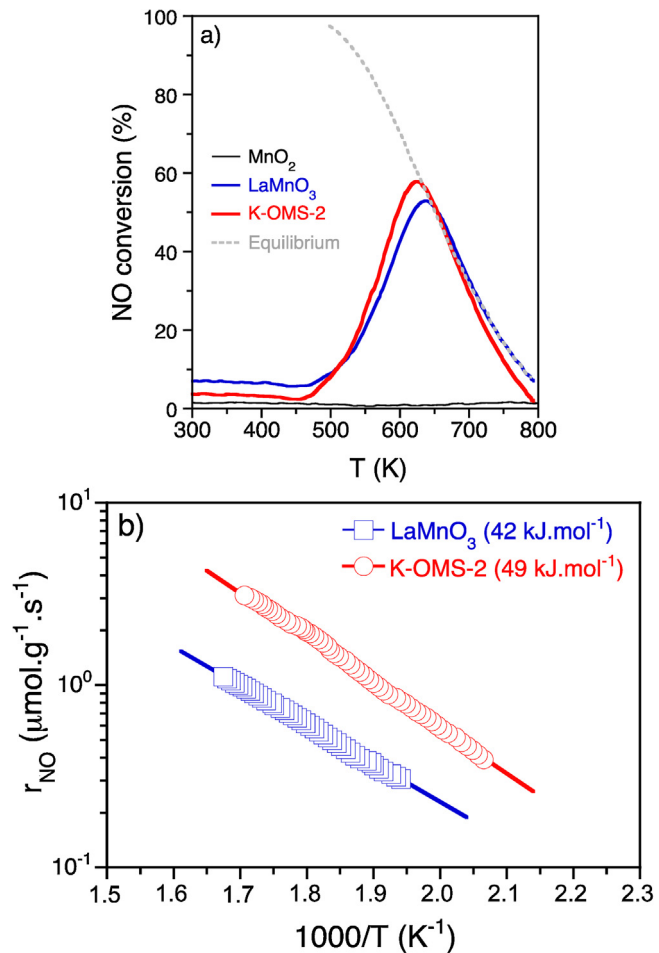


**Fig. 5.** Catalytic activity in NO oxidation for K-OMS-2, LaMnO<sub>3</sub> and MnO<sub>2</sub>. Reaction conditions: NO = 1000 ppm, O<sub>2</sub> = 8%, Ar balance, total flow rate = 10 L(STP).h<sup>-1</sup>. Catalyst weight: 16.0 mg for K-OMS-2, 42.1 mg for LaMnO<sub>3</sub> and 15.1 mg for MnO<sub>2</sub> corresponding to 0.174 mmol Mn for all samples after density correction.

of K-OMS-2, the NO conversion increases in all cases with the temperature until a maximum in the range 600–700 K followed by a fast decline upon reaching thermodynamic equilibrium. The addition of non-noble metals exhibits a negative effect on the catalytic performance compared to the parent K-OMS-2 (Fig. 6a). While K-OMS-2 shows a maximum NO conversion of about 58% at 625 K, the catalysts loaded with Fe and Zn yield a maximum conversion of 34% and 37%, respectively, at a slightly higher temperature (642 K and 658 K). In the case of Cu/K-OMS-2, the maximum NO conversion is only 24% at 679 K.

The Arrhenius plots reveal a pronounced decrease of the activation energy for NO oxidation upon addition of Fe, Cu or Zn compared to the parent K-OMS-2, showing values in the narrow range 26–30 kJ mol<sup>-1</sup> (Fig. 6b), which are slightly lower than the values reported in the literature for Cu and Fe-incorporating zeolites (e.g., Cu/SSZ-13, Cu/CHA, Fe/ZSM-5) [53,54]. The incorporation of Fe, and in a lower extend Zn, exerts a positive effect on the reaction rate at low temperatures (<512 K), whereas at higher temperatures the parent K-OMS-2 shows systematically higher reaction rates. Activation energy calculations revealed that kinetics of Cu, Fe and Zn/K-OMS-2 was less sensitive to temperature changes than that of parent K-OMS-2. As the addition of non-noble metals led to a partial blockage of Mn active sites (as observed by N<sub>2</sub> adsorption-desorption analyses), metal-doped K-OMS-2 catalysts presented less Mn active sites and therefore were less active than K-OMS-2 at higher temperatures. In particular, the reaction rate

**Table 2**Summary of catalytic results<sup>a</sup>.

Sample	M/K-OMS-2							
	Parent	M = Fe	M = Cu	M = Zn	M = Pt	M = Pd	M = Ru	M = Ag
T <sub>20</sub> (K)	541	556	640	571	516	537	498	541
T <sub>max</sub> (K)	624	648	673	654	625	645	584	636
X <sub>NO,max</sub> (%)	58%	34%	24%	37%	54%	43%	75%	48%
r <sub>NO</sub> (T <sub>max</sub> ) (μmol g <sup>-1</sup> s <sup>-1</sup> )	4.1	2.4	1.7	2.6	3.8	3.0	5.3	3.4

<sup>a</sup> Experimental conditions: NO = 1000 ppm, O<sub>2</sub> = 8%, Ar balance, total flow rate = 10 L(STP).h<sup>-1</sup>, GHSV = 35,000 h<sup>-1</sup>, 16 mg catalyst (0.174 mmol Mn).

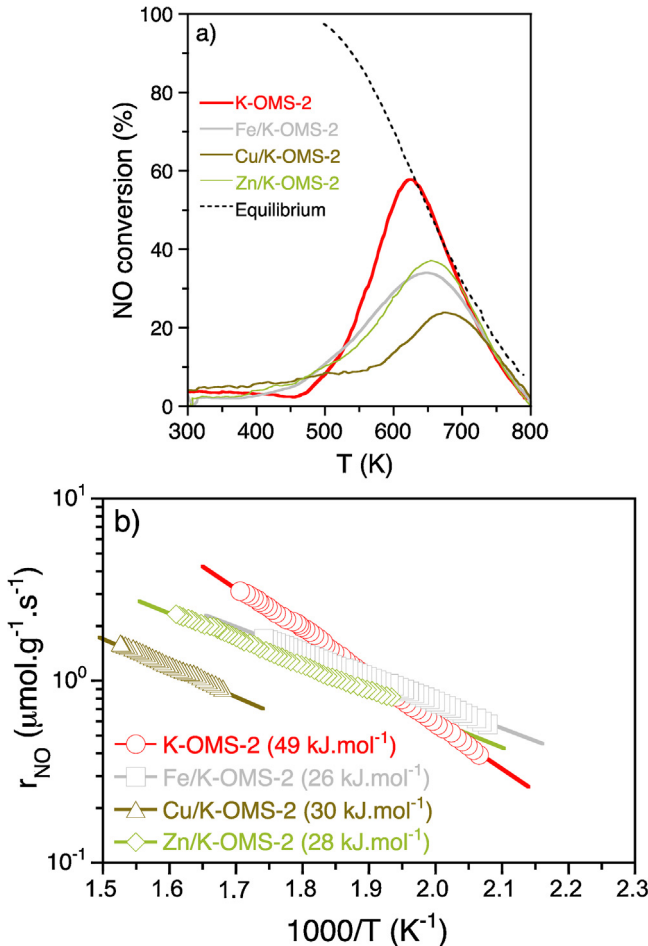


**Fig. 6.** a) Catalytic activity in NO oxidation for raw K-OMS-2 and K-OMS-2 loaded with non-noble metals (16 mg, 0.174 mmol Mn), and b) corresponding Arrhenius plots. Reaction conditions as in.

measured at the maximum temperature exhibits an almost 50% decrease for the different metal-supported catalysts compared to the reaction rate measured on K-OMS-2 (Table 2). Finally, note that in the case of Cu/K-OMS-2, the temperature range for Arrhenius behavior shifts to much higher temperatures, which is consistent with the lower activity observed for this catalyst.

### 3.2.3. Effect of noble metals on the catalytic activity of K-OMS-2

The addition of noble metals to K-OMS-2 results in no appreciable change of the NO conversion in most cases, compared to K-OMS-2 (Fig. 7a). Pt/K-OMS-2 shows a maximum NO conversion of 54% at 626 K with a slightly higher activity in the low temperature range (450–600 K) compared to K-OMS-2. After Pd or Ag addition, the activity of the resultant catalysts is surprisingly lower than that of K-OMS-2 with a NO conversion up to 42% and 48%, respectively, and peak maxima in each case located at 642 K and 633 K. Opposing this behavior, Ru/K-OMS-2 displays a much higher NO conversion

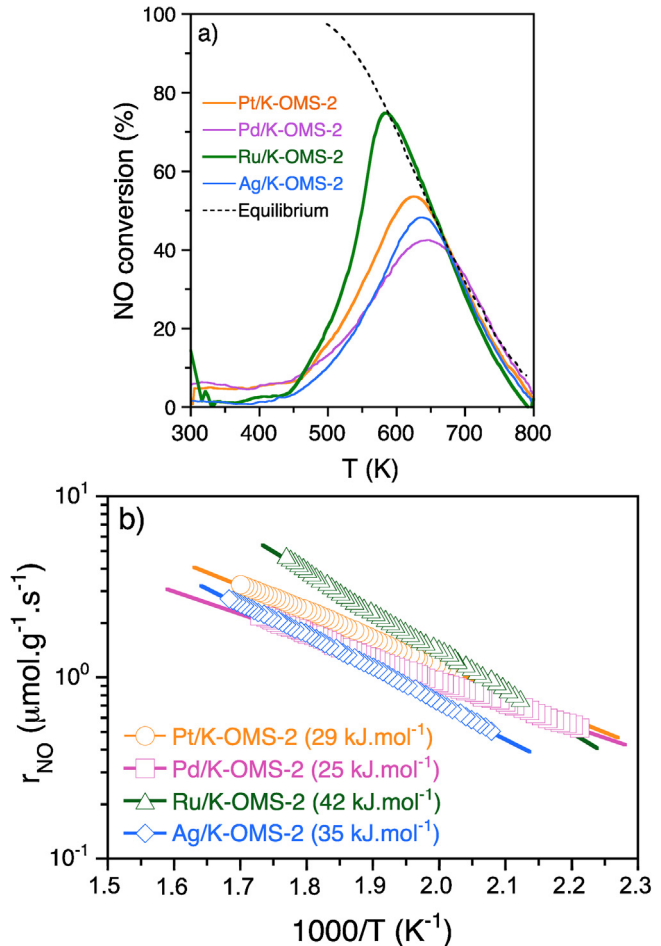


**Fig. 7.** a) Catalytic activity in NO oxidation for raw K-OMS-2 and K-OMS-2 loaded with noble metals (16 mg, 0.174 mmol Mn), and b) corresponding Arrhenius plots. Reaction conditions as in Fig. 5.

(75%) at a comparatively lower temperature (584 K), reflecting a synergistic effect of Ru together with K-OMS-2 on the catalytic activity. A more clear insight into the positive effect of Ru on the NO oxidation properties of K-OMS-2 can be gained by comparing the reaction temperature needed to reach 20% NO conversion (*i.e.* T<sub>20</sub>). Table 2 lists the values measured for the different catalysts. Overall, Ru/K-OMS-2 shows the lowest reaction temperature (498 K), whereas the parent K-OMS-2 requires 541 K. On the other hand, Cu/K-OMS-2 is the catalyst that needs the highest temperature (640 K).

Unlike non-noble metals, the Arrhenius plots reveal only a modest decline in the activation energy for Ru/K-OMS-2 and Ag/K-OMS-2 with values about 42 kJ mol<sup>-1</sup> and 35 kJ mol<sup>-1</sup>, respectively, whereas the decline is more drastic for Pt/K-OMS-2 and Pd/K-OMS-2 (29 kJ/mol and 25 kJ mol<sup>-1</sup>, respectively) (Fig. 7b). Noteworthy, the activation energy for Pt/K-OMS-2 is 25% lower than the values measured on benchmark Pt-supported samples (*e.g.*, Pt/Al<sub>2</sub>O<sub>3</sub>,

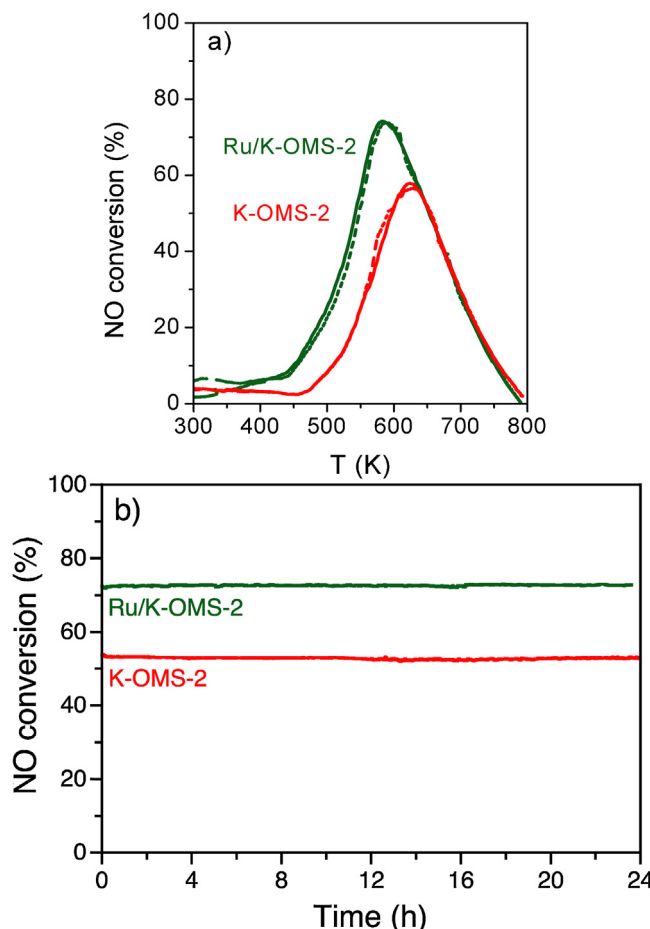


**Fig. 8.** a) Catalytic stability for K-OMS-2 and Ru/K-OMS-2 (16 mg, 0.174 mmol Mn) in NO oxidation for two consecutive cycles, and b) catalytic stability during 24 h continuous operation at 570 and 600 K for K-OMS-2 and Ru/K-OMS-2, respectively. Operating reaction conditions as in Fig. 5.

Pt/SiO<sub>2</sub>) [55,56]. The incorporation of noble metals impacts to an important extent on the catalytic activity at lower temperatures, showing higher catalytic activities compared to the parent K-OMS-2, especially for Pt/K-OMS-2 and Ru/K-OMS-2. This latter catalyst also exhibits the highest reaction rate for NO oxidation at the maximum reaction temperature, with a value of 5.3 μmol g<sup>-1</sup> s<sup>-1</sup>, which is about 25% higher than the reaction rate measured on K-OMS-2 (Table 2).

Catalysis for NO oxidation towards NO<sub>2</sub> on noble metal catalysts is known to be particle-size dependent with the catalytic activity increasing with the particle size in the case of Pt [57,58] and Pd [59]. In our case, no clear correlation can be deduced between the OMS particle size and the catalytic activity. Notwithstanding this fact, the order of catalytic activity observed for noble metal catalysts can be directly linked with the H<sub>2</sub> consumption (Table 1), which is related to the reducible Mn(IV) cations in the K-OMS-2 framework: (Ru/K-OMS-2 > Pt/K-OMS-2 ≈ K-OMS-2 > Ag/K-OMS-2 ≈ Pd/K-OMS-2). This last catalyst was not characterized by TPR in the present work, so the H<sub>2</sub> consumption is not reported here. However, the value of this parameter for a similar catalyst was reported elsewhere [34], showing a H<sub>2</sub> consumption slightly higher than that of the parent K-OMS-2, what could be in contradiction with the order of catalytic activity observed in the present work. The high catalytic performance of Ru-loaded catalysts in the NO oxidation reaction is consistent with reported studies using Ru as active phase, either alone [60], or in bimetallic catalysts [61]. Accordingly, the promising catalytic results obtained

for Ru/K-OMS-2 can be attributed not only to a higher reducibility of the K-OMS-2 support upon addition of Ru, but also to the contribution of this metal to the catalytic activity, as finely dispersed and amorphous RuO<sub>2</sub> species have been identified to be very active in the NO oxidation reaction [60].

### 3.2.4. Catalyst stability

Given the prominent catalytic activity observed on Ru/K-OMS-2, a dedicated study on the stability of this catalyst was conducted and compared to that of K-OMS-2. In this test, the catalysts were subjected to two consecutive catalytic cycles with an intermediate stabilization at the maximum temperature for 24 h. As inferred from Fig. 8, both Ru/K-OMS-2 and the parent K-OMS-2 show identical conversion-temperature curves after the first catalytic cycle. Furthermore, during the 24-h stabilization period, the NO conversion shows almost negligible fluctuation, reflecting the high stability of the catalyst during operation.

## 4. Conclusions

The addition of different non-noble and noble metals to cryptomelane (K-OMS-2) has been evaluated for NO oxidation. The metal-loaded catalysts by the ion-exchange method reveal no remarkable changes in neither the textural nor morphological properties compared to the parent K-OMS-2. However, noble metals clearly impact the redox behavior and the reducibility of the catalysts following the order Ru/K-OMS-2 > Pt/K-OMS-2 > K-OMS-2 > Ag/K-OMS-2. The parent K-OMS-2 reveals an intrinsically high catalytic activity for NO oxidation, reaching a conversion of 58% at the maximum reaction temperature (624 K). The addition of non-noble metals exerts a detrimental effect in the catalytic activity, especially in the case of Cu/K-OMS-2. In contrast, an enhancement of the catalytic activity by 20% is observed after addition of Ru, the NO conversion attaining a value up to 75% at 584 K. The enhanced catalytic properties of Ru/K-OMS-2 can be most likely attributed to a higher reducibility of this catalyst. Ru/K-OMS-2 shows promising credentials for partial NO oxidation into NO<sub>2</sub> in view of fast SCR applications.

## Acknowledgements

This work was initiated and supported by the “Région Auvergne Rhône Alpes” (Coopera project 113955/2015) in a joint research program between the *Institut de Recherches sur la Catalyse et l’Environnement de Lyon* (Univ Lyon, UMR 5256 CNRS/UCBL1), the *Eco-Efficient Products and Process Laboratory* (UMI 3464 CNRS/Solvay) and the *East China University of Science and Technology*. Also a part of this experimental study was supported by the National Basic Research Program of China (2013CB933200), the National Natural Science Foundation of China (21577034) and the 111 project (B08021).

## References

- [1] Integrated Science Assessment for Oxides of Nitrogen and Sulfur -Ecological Criteria US, EPA, EPA/600/R-08/082F, 2008.
- [2] Integrated Science Assessment for Oxides of Nitrogen and Sulfur—Health Criteria, US, EPA, EPA/600/R-15/068, 2016.
- [3] G. Centi, S. Perathoner, *Stud. Surf. Sci. Catal.* 171 (2007) 1–23.
- [4] M.F. Irfan, J.H. Goo, S.D. Kim, *Appl. Catal. B: Environ.* 78 (2008) 267–274.
- [5] B. Guan, R. Zhan, H. Lin, Z. Huang, *Appl. Therm. Eng.* 66 (2014) 395–414.
- [6] Y.F. Shen, R.P. Zerger, R.N. DeGuzman, S.L. Suib, L. McCurdy, D.I. Potter, C.L. O’Young, *Science* 260 (1993) 511–515.
- [7] J. Liu, V.D. Makwana, J. Cai, S.L. Suib, M. Aindow, *J. Phys. Chem. B* 107 (2003) 9185–9194.
- [8] S.L. Suib, *Acc. Chem. Res.* 41 (2008) 479–487.
- [9] Y.F. Shen, S.L. Suib, C.L. O’Young, *J. Am. Chem. Soc.* 116 (1994) 11020–11029.
- [10] J. Luo, Q. Zhang, J. Garcia-Martinez, S.L. Suib, *J. Am. Chem. Soc.* 130 (2008) 3198–3207.

[11] J. Luo, Q. Zhang, A. Huang, S.L. Suib, *Microporous Mesoporous Mater.* 35–36 (2000) 209–217.

[12] R. Hu, Y. Cheng, L. Xie, D. Wang, *Chin. J. Catal.* 28 (2007) 463–468.

[13] J. Chen, J. Li, H. Li, X. Huang, W. Shen, *Microporous Mesoporous Mater.* 116 (2008) 586–592.

[14] W.Y. Hernandez, M.A. Centeno, S. Ivanova, P. Eloy, E.M. Gagneaux, J.A. Odriozola, *Appl. Catal. B: Environ.* 123–124 (2012) 27–35.

[15] A.R. Gandhe, J.S. Rebello, J.L. Figueiredo, J.B. Fernandes, *Appl. Catal. B: Environ.* 72 (2007) 129–135.

[16] V.P. Santos, M.F.R. Pereira, J.J.M. Órfão, J.L. Figueiredo, *Appl. Catal. B: Environ.* 88 (2009) 550–556.

[17] H. Sun, S. Chen, P. Wang, X. Quan, *J. Chem. Eng.* 178 (2011) 191–196.

[18] O. Sanz, J.J. Delgado, P. Navarro, G. Arzamendi, L.M. Gandía, M. Montes, *Appl. Catal. B: Environ.* 110 (2011) 231–237.

[19] M. Sun, L. Yu, F. Ye, G. Diao, Q. Yu, Z. Hao, Y. Zheng, L. Yuan, *J. Chem. Eng.* 220 (2013) 320–327.

[20] Y.-C. Son, V.D. Makwana, A.R. Howell, S.L. Suib, *Angew. Chem. Int. Ed.* 40 (2001) 4280–4283.

[21] V.D. Makwana, Y.-C. Son, A.R. Howell, S.L. Suib, *J. Catal.* 210 (2002) 46–52.

[22] V.D. Makwana, L.J. Garces, J. Liu, J. Cai, Y.C. Son, S.L. Suib, *Catal. Today* 85 (2003) 225–233.

[23] R. Kumar, S. Sithambaram, S.L. Suib, *J. Catal.* 262 (2009) 304–313.

[24] R. Jothiramalingam, B. Viswanathan, T.K. Varadarajan, *J. Mol. Catal. A: Chem.* 252 (2006) 49–55.

[25] K.A. Malinger, Y.-S. Ding, S. Sithambaram, L. Espinal, S. Gomez, S.L. Suib, *J. Catal.* 239 (2006) 290–298.

[26] G.D. Yadav, R.K. Mewada, *Chem. Eng. Res. Des.* 90 (2012) 86–97.

[27] L. Espinal, S.L. Suib, J.F. Rusling, *Electrochemical catalysis of styrene epoxidation with films of MnO<sub>2</sub> nanoparticles and H<sub>2</sub>O<sub>2</sub>*, *J. Am. Chem. Soc.* 126 (2004) 7676–7682.

[28] R. Ghosh, Y.-C. Son, V.D. Makwana, S.L. Suib, *J. Catal.* 224 (2004) 288–296.

[29] R. Ghosh, X. Shen, J.C. Villegas, Y. Ding, K. Malinger, S.L. Suib, *Role of manganese oxide Octahedral Molecular Sieves in styrene epoxidation*, *J. Phys. Chem. B* 110 (2006) 7592–7599.

[30] H. Nur, F. Hayati, H. Hamdan, *Catal. Commun.* 8 (2007) 2007–2011.

[31] G.D. Yadav, R.K. Mewada, *Catal. Today* 198 (2012) 330–337.

[32] H.G. Manyar, B. Yang, H. Daly, H. Moor, S. McMonagle, Y. Tao, G.D. Yadav, A. Goguet, P. Hu, C. Hardacre, *ChemCatChem* 5 (2013) 506–512.

[33] H. Sun, Z. Liu, S. Chen, X. Quan, *J. Chem. Eng.* 270 (2015) 58–65.

[34] M. Ousmane, G. Perrussel, Z. Yan, J.-M. Clacens, F. De Campo, M. Pera-Titus, *J. Catal.* 309 (2014) 439–452.

[35] T. Martínez, L.M. Arzamendi, F. Romero-Sarria, W.Y. Hernández, M.A. Centeno, J.A. Odriozola, *Applied Catal. A: Gen.* 423–424 (2012) 137–145.

[36] Z.-Y. Cai, M.-Q. Zhu, J. Chen, Y.-Y. Shen, J. Zhao, Y. Tang, X.-Z. Chen, *Catal. Commun.* 12 (2010) 197–201.

[37] C.K. King'ondu, N. Opembe, C.-H. Chen, K. Ngala, H. Huang, A. Iyer, H.F. Garces, S.L. Suib, *Adv. Funct. Mater.* 21 (2011) 312–323.

[38] X. Chen, Y.F. Shen, S.L. Suib, C.L. O'Young, *J. Catal.* 197 (2001) 292–302.

[39] W.Y. Hernandez, M.A. Centeno, F. Romero-Sarria, S. Ivanova, M. Montes, J.A. Odriozola, *Catal. Today* 157 (2010) 160–165.

[40] J. Cai, J. Liu, W.S. Willis, S.L. Suib, *Chem. Mater.* 13 (2001) 2413–2422.

[41] T. Hamaguchi, T. Tanaka, N. Takahashi, Y. Tsukamoto, N. Takagi, H. Shinjoh, *Appl. Catal. B: Environ.* 193 (2016) 234–239.

[42] W. Huang, J. Shi, *Appl. Catal. A: Gen.* 507 (2015) 65–74.

[43] Z.-M. Wang, S. Tezuka, H. Kanoh, *Chem. Mater.* 13 (2001) 530–537.

[44] Z.-M. Wang, S. Tezuka, H. Kanoh, *NH<sub>3</sub> desorption and decomposition behaviour on microporous hollandite-type hydrous manganese oxide*, *Catal. Today* 68 (2001) 111–118.

[45] L. Sun, Q. Cao, B. Hu, J. Li, J. Hao, G. Jing, X. Tang, *Appl. Catal. A: Gen.* 393 (2011) 323–330.

[46] L. Yun, Y. Li, C. Zhou, L. Lan, M. Zeng, M. Mao, H. Liu, X. Zhao, *Appl. Catal. A: Gen.* 530 (2017) 1–11.

[47] G.G. Xia, W. Tong, E.N. Tolentino, N.-G. Duan, S.L. Brock, J.-Y. Wang, S.L. Suib, T. Ressler, *Chem. Mater.* 13 (2001) 1585–1592.

[48] S. Dharmarathna, C.K. King'ondu, W. Pedrick, L. Pahalagedara, S.L. Suib, *Chem. Mater.* 24 (2012) 705–712.

[49] X.S. Liu, Z.N. Jin, J.Q. Lu, X.X. Wang, M.F. Luo, *J. Chem. Eng.* 162 (2010) 151–157.

[50] Z.Q. Zou, M. Meng, Y.Q. Zha, *J. Phys. Chem. C* 114 (2010) 468–477.

[51] S.J. Gentry, N.W. Hurst, A. Jones, *J. Chem. Soc. Faraday Trans.* 77 (1981) 603–619.

[52] J. Chen, M. Shen, X. Wang, G. Qi, J. Wang, W. Li, *Appl. Catal. B: Environ.* 134–135 (2013) 251–257.

[53] A.A. Verma, S.A. Bates, T. Anggara, C. Paolucci, A.A. Parekh, K. Kamasamudram, A. Yezersets, J.T. Miller, W.N. Delgass, W.F. Schneider, F.H. Ribeiro, *J. Catal.* 312 (2014) 179–190.

[54] P.S. Metkar, V. Balakotaiah, M.P. Harold, *Catal. Today* 184 (2012) 115–128.

[55] S.S. Mulla, N. Chen, W.N. Delgass, W.S. Epling, F.H. Ribeiro, *Catal. Lett.* 100 (2005) 267–270.

[56] R. Marques, P. Darcy, P. Da Costa, H. Mellottée, J.-M. Trichard, G. Djéga-Mariadassou, *J. Mol. Catal. A: Chem.* 221 (2004) 127–136.

[57] P. Denton, A. Giroir-Fendler, H. Praliaud, M. Primet, *J. Catal.* 189 (2000) 410–420.

[58] E. Xue, K. Seshan, J. Ross, *Appl. Catal. B: Environ.* 11 (1996) 65–79.

[59] B.M. Weiss, E. Iglesia, *J. Catal.* 272 (2010) 74–81.

[60] L. Li, L. Qu, J. Cheng, J. Li, Z. Hao, *Appl. Catal. B: Environ.* 88 (2009) 224–231.

[61] Z. Chen, X. Wang, Y. Wang, R. Wang, *J. Mol. Catal. A: Chem.* 396 (2015) 8–14.